Experimental Thermal and Fluid Science 98 (2018) 346–361

Contents lists available at ScienceDirect

Experimental Thermal and Fluid Science

journal homepage: www.elsevier.com/locate/etfs

R245fa condensation heat transfer in a phase separation condenser

Shuang Cao[a], Xianbing Ji[a], Jinliang Xu[a,b,*]

[a] The Beijing Key Laboratory of Multiphase Flow and Heat Transfer, North China Electric Power University, Beijing 102206, China
[b] Key Laboratory of Condition Monitoring and Control for Power Plant Equipment of Ministry of Education, North China Electric Power University, Beijing 102206, China

ARTICLE INFO

Keywords:
Condensation
Heat transfer
R245fa
Phase separation

ABSTRACT

The R245fa condensation heat transfer is investigated in a phase separation shell-tube condenser with mesh tubes inserted. The condenser has three copper tubes which have an inner diameter of 14.70 mm and a heat transfer length of 1600 mm. Four mesh tubes with mesh pore width of 15 μm are arranged in each copper tube. The comparative experiments are conducted for condensers with or without mesh tubes inserted. The flow pattern visualization is investigated to explore heat transfer enhancement mechanisms. The results showed that, with vapor mass qualities and mass fluxes increased, condensation heat transfer coefficients and friction pressure drops are increased, but heat transfer enhancement ratios and performance evaluation parameters are decreased. At low mass fluxes, the heat transfer coefficients behave a slow decrease trend with increase of inclination angles. The pressure difference between annular region and core region drives liquid flow towards core region, reducing liquid film thickness on tube bottom and increasing vapor void fractions near tube wall. With increase of inclination angles, the pressure difference is reduced but liquid film thickness on tube bottom is increased. For horizontal flow, there is an optimal match between pressure difference of annular region and core region and liquid-mesh tube contact area. Under such circumstance, the heat transfer enhancement ratios reach maximum.

1. Introduction

Condenser is a kind of heat exchangers, which condenses pure vapor or vapor-liquid mixture into saturation or subcooled liquid by dissipating heat to a cooling medium. The cooling medium can be air, water or any other fluid. Condensers have wide industry applications such as air conditioning, refrigeration, and Rankine cycle power plant etc.

Recently, organic Rankine cycle (ORC) technology is considered as a practical solution to convert low grade heat source into electricity because of its simplicity, reliability and flexibility [1–3]. ORCs employ organic fluids with low boiling points (such as R123) instead of water as the working fluid. The organic liquid is pumping into an evaporator to generate high pressure working fluid vapor which drive a turbine to produce power. Then, the low pressure vapor at the turbine outlet is condensed to liquid in a condenser. However, one of the main problems in ORCs is the large size and high investment cost. Due to the lower specific heats, thermal conductivities and latent heat, the phase change heat transfer coefficients of organic fluids are even lower than the forced convective heat transfer coefficients of water [4]. Enhancing the phase change heat transfer in condenser could significantly reduce the size and investment cost of ORCs.

Considerable attention has been focused on enhancing condensation heat transfer. Modulated tubes, such as microgroove tubes [5,6], microfin tubes [7,8], corrugated tubes [9,10] and herringbone tubes [11], can be expected to have excellent heat transfer performance. These techniques extend the heat transfer surface and intensify the fluid turbulence. Generally, for the vapor-liquid two-phase flow in tubes, the vapor phase tends to accumulate in the tube core and the liquid phase tends to stick on the tube wall. The thick liquid film separates the saturated vapor from the tube wall and also induces a large thermal resistance. Such vapor-liquid phase distribution weakens the condensation heat transfer in tubes. However, the previous techniques do not involve the flow pattern modulation in tubes.

To modulate flow patterns in tubes, our group proposed the passive phase separation concept [12,13]. An empty mesh cylinder was suspended in a tube to create a distinct phase distribution in the tube cross section. The mesh surface prevents vapor phase entering the mesh cylinder thus the vapor flows in the annular section. The liquid phase can be sucked into the mesh cylinder through the miniature pores of the mesh surface by capillary force. Thus, the vapor phase mainly populated near the tube wall region and the liquid phase tends to accumulate in the tube core, which could significantly enhance the condensation heat transfer in tubes. Subsequently, the experimental and numerical tests were conducted on phase separation tubes. Sun et al. [14,15] proposed a numerical simulation of the bubble dynamics for a single

* Corresponding author at: The Beijing Key Laboratory of Multiphase Flow and Heat Transfer, North China Electric Power University, Beijing 102206, China.
E-mail address: xjl@ncepu.edu.cn (J. Xu).

https://doi.org/10.1016/j.expthermflusci.2018.06.022
Received 16 April 2018; Received in revised form 16 June 2018; Accepted 22 June 2018
Available online 23 June 2018
0894-1777/

Nomenclature

A	annular flow
AC	alternative current
BTC	bare tube condenser
C_p	specific heat at constant pressure, J/kg·K
d	diameter, m
E	surface energy, J/m
EF	heat transfer enhancement ratio
G	mass flux, kg/m^2 s
g	gravity force, m/s^2
h	heat transfer coefficient, W/m^{2}K
h_l	liquid height, m
i	enthalpy, J/kg
I	current, A
I	intermittent flow
K	porous permeability
k	thermal conductivity, W/(mK)
L	length, m
$LMTD$	logarithmic mean temperature difference, °C or K
m	mass flow rate, kg/s
N	number of mesh pores
n	number of data points
P	pressure, Pa
PEC	performance evaluation parameter
PSC	phase separation condenser
ΔP	pressure drop, Pa
q	heat flux on the inner wall surface, W/m^2
Q	heat transfer rate, W
S	tube circumference length, m
SS	stratified-smooth flow
SW	stratified-wavy flow
t	time, s
T	temperature, °C or K
U	voltage, V
u	velocity, m/s
w	width of the mesh pore, m
x	vapor mass quality

Greek symbols

α	wetting angle, °
θ	inclination angle, °
η	thermal efficiency
μ	viscosity, pa/s
ρ	density, kg/m^3
σ	surface tension, N/m
ϕ_l^2	two-phase flow multiplier

Subscript

au	annular region
A	cross section A-A
ave	average
B	cross section B-B
bw	bottom wall location
c	cooling water
cb	cooling water bottom corner
cl	cooling water left corner
co	core region
cr	cooling water right corner
con	condenser
e	effective heat transfer
eva	evaporator
f	frictional pressure
g	vapor
i	inside wall surface
in	condenser inlet
l	liquid
m	mean
max	maximum
min	minimum
o	outer wall surface
out	condenser outlet
r	organic fluid (R245fa in this study)
sw	side wall location
tw	top wall location
to	total
w	wall

bubble in the vertical phase separation condenser tube. The results showed zero void fractions inside the mesh cylinder and higher gas void fractions near the tube wall. Liquid film thicknesses can be reduced by 70% compared to that in the bare tube region. Xing et al. [16] investigated the single phase heat transfer in a vertical upward phase separation tube. They found the heat transfer was enhanced over the whole tube, with the heat transfer enhancement ratios from 1.21 to 1.84, and the largest enhancement ratio occurred in the transition flow regime. Xie et al. [17] investigated R123 condensation heat transfer in a horizontal tube with an inside diameter of 14.81 mm. The mesh cylinder was formed by packaging two layers of mesh screen surface. The results showed that the heat transfer coefficients of horizontal tube with mesh tube inserted had more than 2 times that of tube without mesh tube.

Many studies focused on the flow patterns and condensation heat transfer in bare tubes at inclined angles. Lips and Meyer [18] investigated the effect of inclination angles on the condensation heat transfer and flow patterns in a 8.38 mm inner diameter smooth tube. They showed that heat transfer coefficient was strongly affected by the liquid layer thickness at the tube bottom for stratified flows. Nitheanandan and Soliman [19] examined the effect of inclination angles on the flow regime boundaries in a 13.4 mm inner diameter copper tube. They found that inclination angles had a strong influence on the wavy and slug flow, but the effect was almost insignificant on the annular flow. Mohseni et al. [20] investigated the flow patterns and heat transfer of R134a in a bare tube, they found that maximum condensation heat transfer coefficients occurred at $\theta = 30^\circ$ (upflow) for low vapor mass qualities but at $\theta = 0^\circ$ (horizontal flow) with high vapor mass qualities. Our previous work [21,22] had shown that the horizontal position yielded the minimum condensation heat transfer coefficients for the bare tube. The deviation from the horizontal position would enhance condensation heat transfer. The mechanisms to enhance condensation heat transfer were the decreased liquid film thickness on the tube bottom for inclined downflow and the increased vapor-liquid interface fluctuation strength for inclined upflow. However, studies on phase-change heat transfer in the modulated heat transfer tube are not enough. The test of a porous-membrane-tube decorated into the copper tube was proposed by Xie et al. [23]. It was found that modulated heat transfer tube had 85% improvement of condensation heat transfer coefficients than the bare tube, maximally. The liquid flow to porous-membrane-tube and the decreased liquid height in the annular region are the heat transfer enhancement mechanism for annular flow and stratified flow modulation, respectively. The smallest condensation heat transfer coefficients occurred in the horizontal flow. The vertical upflow had the largest condensation heat transfer coefficients, due to the increased liquid mass and momentum

exchange across the porous membrane. Until now, the effect of slightly inclined angles on condensation heat transfer in phase separation tube was not reported.

In summary, it was not deeply understood about the mechanism of the slightly inclined angle effects on the condensation heat transfer in modulated tube by using the phase separation concept. This paper investigated condensation heat transfer in a phase separation shell-tube condenser with mesh tubes inserted. The condenser was tested at slightly inclined angles from −30° (inclined downflow) to 30° (inclined upflow). R245fa, which has zero ozone depletion potential (ODP) and lower global warming potential (GWP) than other refrigerants [24], was used as the working fluid. Attention was paid to explain the influence of mass fluxes, vapor mass qualities and inclination angles on the condensation heat transfer coefficients. Flow visualization, pressure balance analysis and dynamic liquid height were measured to explore the heat transfer enhancement mechanisms. This paper was organized as follows: Section 2 presented the design and working principle of modulated tube with mesh tubes inserted. Section 3 described experimental details, including experimental setup, test section, data reduction and uncertainty analysis, and calibration experiment. Section 4 reported the results and discussion. Finally, the main conclusions were summarized in Section 5.

2. The modulated tube design and working principle

Fig. 1a shows the design of phase separation modulated tube. An empty mesh cylinder is welded to the support structures, ensuring the mesh cylinder is suspended in the condenser tube. The entrance of mesh cylinder is just a flat mesh surface, but the exit is open to discharge the separated liquid. The mesh cylinder surface divides the condenser tube into an annular region and a core region. When a vapor-liquid two-phase flow approaches the mesh cylinder region, the mesh pores

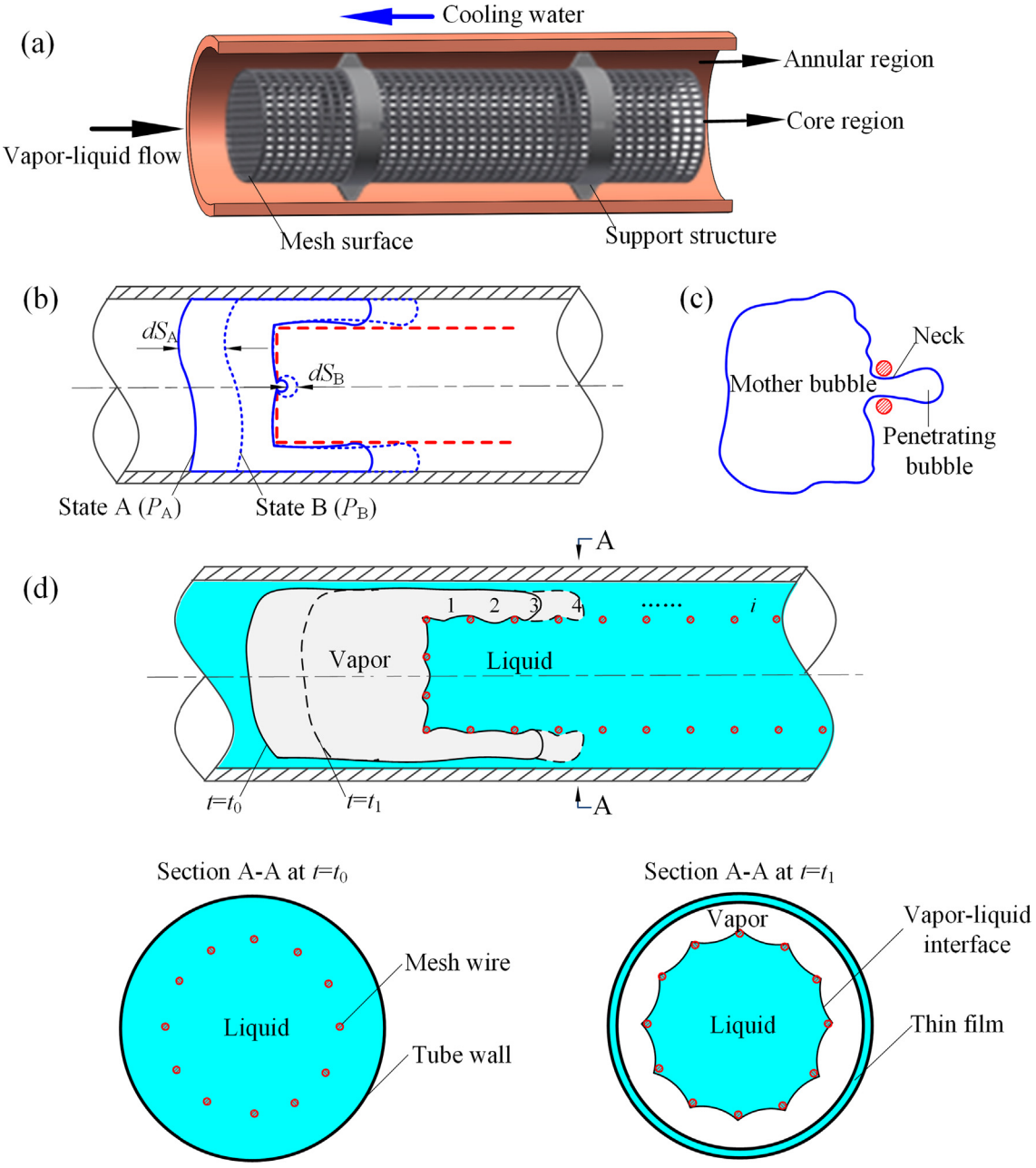

Fig. 1. Design and working principle of phase separation modulated tube ((a) the design of phase separation modulated tube, (b–c) the mechanism of the mesh pores preventing bubbles entering the mesh cylinder and (d) the liquid suction caused by dynamic process of bubble front sweeping the mesh pores).

prevent vapor bubble entering the core region but capture liquid into the core region. Thus, the vapor-liquid phase distribution in condenser tube is successfully modulated. The mesh pore should be small enough to prevent vapor bubble entering the core region and drive liquid towards the core region. An effective pore diameter $d_e < \sqrt{\sigma/g(\rho_l-\rho_g)}$ is suggested by Ref [25], where σ is the surface tension force, g is the gravitational acceleration, and ρ_l and ρ_g are the liquid and vapor densities, respectively. For most vapor-liquid two-phase systems, d_e is of the order of millimeter.

The surface energy of the vapor bubble is increased when it is forced to move from a large space into a small space. When a large bubble with its diameter identical to the condenser tube enters the mesh pore (see Fig. 1b), the surface energy of the bubble between state A and B is:

$$dE = 4\sigma w dS_B - \pi\sigma D dS_A \tag{1}$$

where E is the surface energy, D is the condenser tube inner diameter, w is the width of the mesh pore.

Neglecting the bubble density variation, the mass conservation is:

$$w^2 dS_B = \pi D^2 dS_A/4 \tag{2}$$

The work driving the bubble transform from state A to state B is:

$$dK = P_A \pi D^2 dS_A - P_B w^2 dS_B \tag{3}$$

The dK being equal to dE and combining Eqs. (1) to (3), P_A–P_B can be expressed as:

$$P_A - P_B = 4\sigma\left(\frac{1}{w}-\frac{1}{D}\right) \tag{4}$$

Because D is far greater than w, the second term of the right side of Eq. (4) contributes much less to the pressure difference. Giving σ = 0.00959 N/m for R245fa two-phase fluid at its saturation temperature of 60 °C and w = 0.05 mm, P_A-P_B = 767.2 Pa, indicating that the pressure difference of more than 767.2 Pa is necessary to penetrate the front bubble interface in the mesh pore. However, due to the viscous force from surrounding liquid, penetrating a bubble front over the mesh pore does not mean that such a bubble can successfully separate from its mother bubble and enter the mesh cylinder (see Fig. 1c).

Fig. 1d shows the liquid capturing mechanism of modulated tube. The mesh pores are marked as the index i = 1, 2, 3…along the flow direction. A large bubble with its front traveling ahead in the annular region and consecutively sweeps the mesh pores. At $t = t_0$, the bubble front does not reach the #4 mesh pore, so the cross section A–A is full of liquid. A curved vapor-liquid interface is formed within the #4 mesh pore at $t_1 = t_0 + \Delta t$, where $\Delta t = w/u_g$, u_g is the moving speed of the bubble front in annular region. The cross section A–A has a thin liquid film on the tube wall and a liquid core with curved vapor-liquid interface at $t = t_1$.

Noting that the capillary pressure is changed during the dynamic interface formation process when the bubble front is sweeping the mesh pores. The capillary pressure is zero at $t = t_0$ and it is expressed as $\Delta p_c = 4\sigma\cos\alpha/d_e$ at $t = t_1$ [26], where α is the wetting angle. Based on the Darcy's law, the pressure drop for the liquid flow through mesh pores is $\Delta p_l = \mu_l u_{l,s}\Delta x/K$, where $u_{l,s}$ is the liquid suction velocity through the mesh pores, Δx is the distance for the liquid flow path, K is the porous permeability of the mesh cylinder surface. The Δp_c being equal to Δp_l, thus the liquid suction velocity can be expressed as:

$$u_{l,s} = \frac{4\sigma K\cos\alpha}{\mu_l d_e \Delta x} \tag{5}$$

The total mass flow rate of the liquid suction through mesh pores is:

$$m_{l,s} = \frac{4N\rho_l\sigma w^2 K\cos\alpha}{\mu_l d_e \Delta x} \tag{6}$$

where N is the total number of mesh pores along the circumference direction in the A–A section.

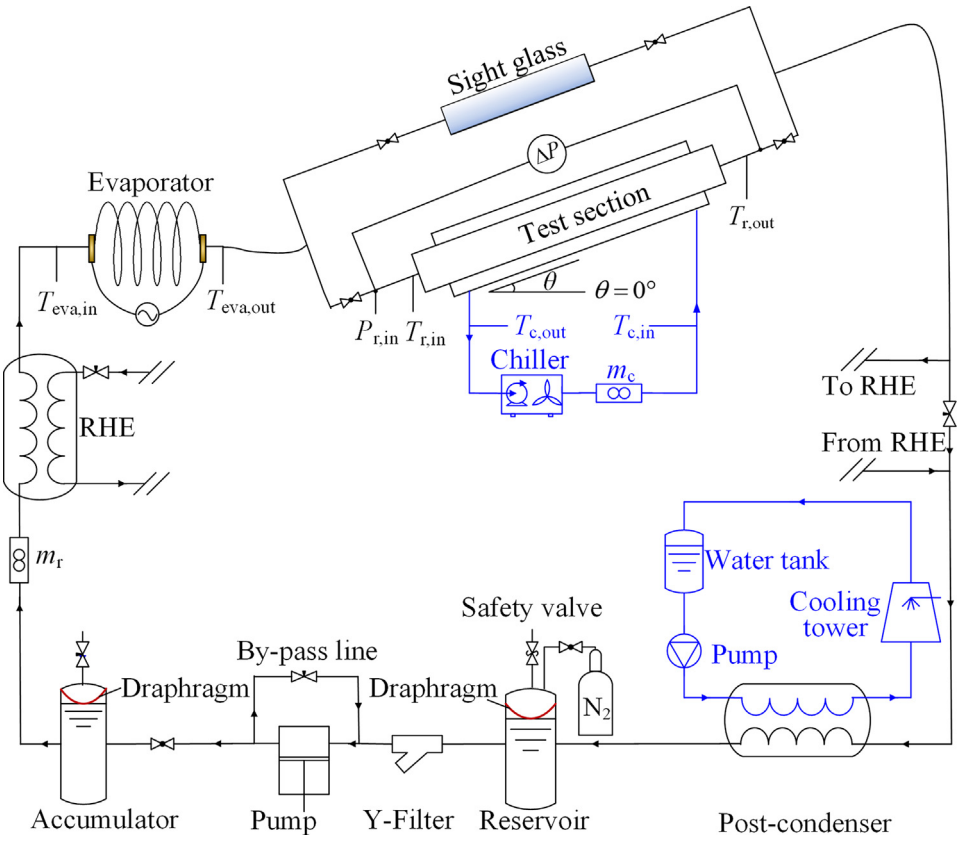

Fig. 2. Experimental setup.

3. Experimental details

3.1. Experimental setup

The schematic diagram of experimental setup is shown in Fig. 2. The system consisted of an R245fa fluid loop, a regenerative heat exchanger (RHE), a serpentine coiled tube evaporator, a shell-tube-condenser test section and its cooling water system, a post-condenser and a cooling water loop. Initially, the R245fa fluid loop was vacuumed to remove non-condensable gas by a vacuum pump and then was charged with R245fa liquid. The R245fa liquid in the reservoir was circulated by a hydraulic diaphragm pump, ensuring no lubrication oil entering the test section. The specified pumping flow rate was controlled by the by-pass valve together with the frequency converter and diaphragm displacement of the pump. An accumulator at the pump outlet was used to avoid oscillation. Specific liquid levels of the reservoir and accumulator were pressurized by the nitrogen gas which was separated by a diagram from R245fa liquid to ensure no-condensable gas in R245fa. R245fa

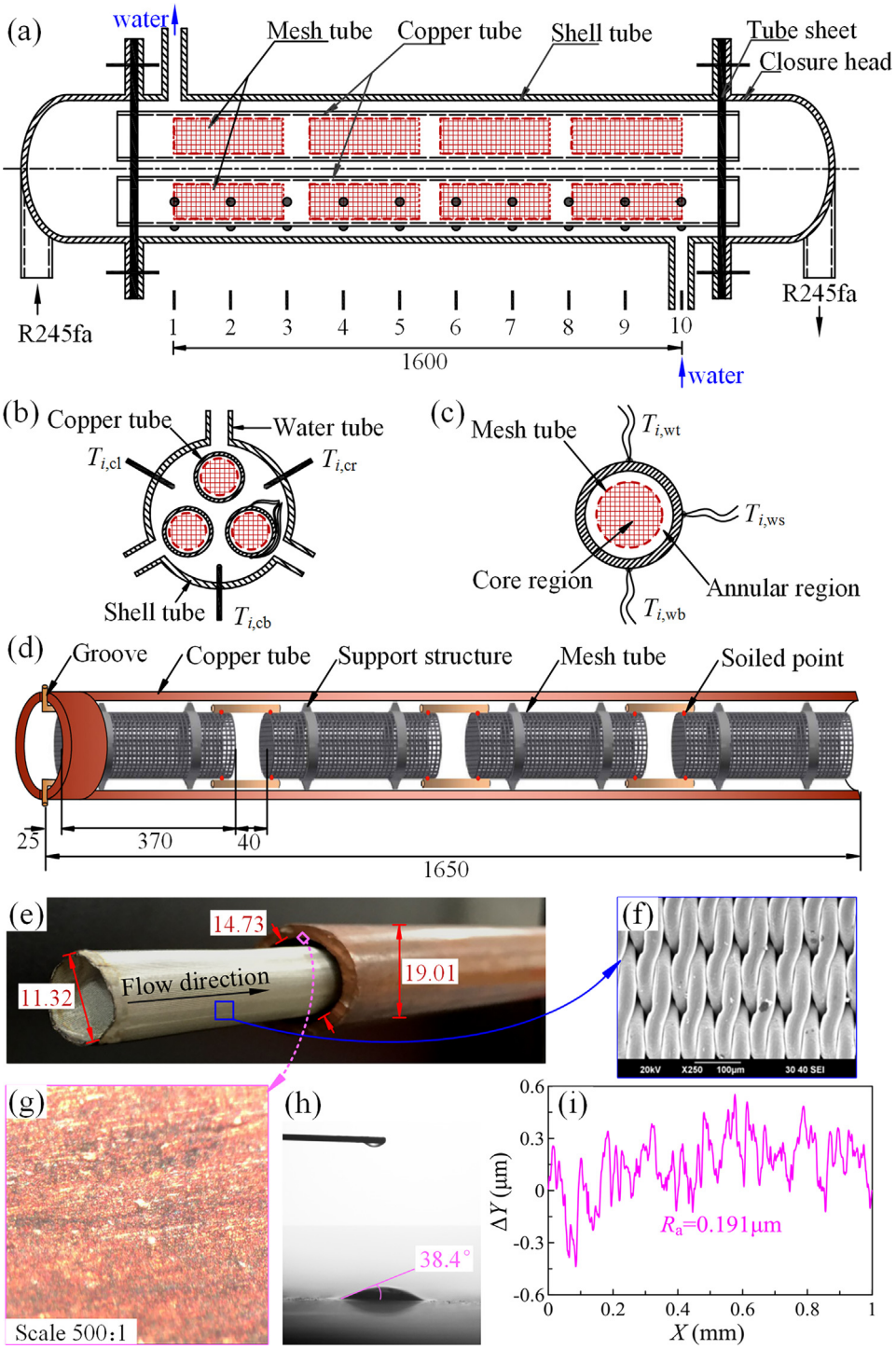

Fig. 3. Test section ((a) phase separation condenser, (b) distribution of temperature measurement points in water, (c) distribution of temperature measurement points on the tube wall, (d) mesh tube installation in the copper tube, (e) mesh tube, (f) SEM image of the mesh screen, SEM image (g), wettability (h) and roughness (i) of the copper tube surface).

pressure at the test section inlet was maintained at about 505 kPa, corresponding to its saturation temperature of 63.1 °C. During the experiments, the good agreement between the measured pressure and saturation temperature also indicated insignificant non-condensable gas in the R245fa liquid.

The R245fa liquid in the serpentine coiled tube evaporator was heated by an *AC* (alternative current) electrical power with a maximum heating power of about 54 kW. The evaporator tube had a stretched length of 20.0 m and was electrically insulated from other components. The heating power can be calculated by measuring voltage and current. The R245fa fluid at the evaporator inlet was subcooled liquid with the temperature ($T_{eva,in}$) and it was heated to the two-phase state at the evaporator outlet with the saturation temperature ($T_{eva,out}$). A regenerative heat exchanger was installed before the evaporator to recover heat from the test section outlet. Then the R245fa fluid was cooled to subcooled liquid in a post-condenser by cooling water. The cooling water was pumped to a closed cooling tower with a maximum cooling capability of 72 kW.

The test section was tightly installed on a special rotating platform with an angle uncertainty of 0.1°. Inclination angles of $\theta = 0°$, positive θ and negative θ refer to the horizontal, inclined up and inclined down flow direction, respectively. A chiller water loop, connected to test section by flexible stainless steel tubes, was used to condense R245fa two-phase fluid in the test section. The loop consisted of an air-cooled chiller, a mass flow meter and two jacket thermocouples. The chiller water flow rate m_c was measured by the mass flow meter. The inlet and outlet temperatures ($T_{c,in}$ and $T_{c,out}$) of the chiller water were measured by the jacket thermocouples. In order to understand the two-phase heat transfer mechanisms, flow visualization studies should be performed. So a smooth quartz glass tube, having identical inside diameter to the copper tube and a total length of 150 mm, was arranged parallel to the test section. The R245fa fluid can be easily switched between the test section and the glass tube by valves. A mesh tube was also inserted in the glass tube. Thus, flow patterns could be obtained by visualization.

3.2. Test section

The test section was a phase separation shell-tube condenser (see Fig. 3a), consisting of three inner copper tubes, twelve short inserted mesh tubes, a shell stainless steel tube and two closure heads. Two tube sheets connected the copper tubes together with the steel tube and closure heads. R245fa two-phase fluid flows inside the copper tubes and cooling water flows in the shell-tube. The condenser had a total length of 1850 mm and an effective heat transfer length of 1600 mm. The steel tube and closure heads had identical inside and outside diameters of 48.50 and 57.08 mm, respectively. Copper tubes had an inside diameter of $d_i = 14.70$ mm and an outside diameter of $d_o = 19.02$ mm. The tube bundles were positioned in a staggered way, with a distance of 21.70 mm between each two copper tubes from center to center.

The flow length of R245fa liquid, 1600 mm, was equally divided into nine parts and has teen cross sections, the distance between two adjacent cross sections was 177.8 mm. Cross sections 1 and 10 refer to the R245fa inlet and outlet, corresponding to cooling water outlet and inlet, respectively, (see Fig. 3a). Three water tubes were symmetrically welded to the shell-tube, ensuring the cooling water homogeneous flowing in the shell-tube. However, no water tubes were arranged on the cross-sections 2–9. On each cross section from 1 to 10, three jacket thermocouples were symmetrically arranged inside the shell-tube (see Fig. 3b), marked as $T_{i,cl}$, $T_{i,cr}$ and $T_{i,cb}$, where i refers to cross section number, subscripts cl, cr and cb refer to left, right and bottom corners of cooling water, respectively. Besides, three thermocouple wires were are arranged on the outside copper tube wall (see Fig. 3c), marked as $T_{i,wt}$, $T_{i,ws}$ and $T_{i,wb}$, where subscripts wt, ws and wb refer to top, side and bottom position of the tube wall, respectively. The thermocouple wires were directly welded on the tube wall by the electro-percussive welding method, thus there is a very little thermal resistance between the thermocouple head and the wall surface. Before the experiment, a large water flow with the temperature of 65 °C was circulated to pass the measured copper tube by the pump of a constant temperature water bath. To reduce heat losses, the tube is covered by 5 cm thickness thermal insulators. The temperature difference between the thermocouple wires and hot water is within 0.8 °C, indicating the measured wall temperatures are accurate enough in this study.

Both the tests were performed on the same condenser with or without the mesh tubes inserted. BTC and PSC refer to the bare tube condenser and the phase separation condenser with mesh tubes inserted, respectively. Fig. 3d shows how the mesh tubes were inserted in the copper tubes. Because liquids will over-sucked into mesh tube if a long inserted mesh tube was used [27], in this paper four short mesh tubes with a length of 370 mm were arranged in each copper tube. Small copper wires were welded to mesh tubes which have an axial distance of 40 mm between two neighboring ones. Two support structures which outside diameters were the same as the inside diameter of copper tubes were also carefully welded to each of mesh tubes. The support structures were tightly stuck on inner wall of copper tubes, ensuring the mesh tubes were suspended in copper tubes and fixed and immovable in radial direction. Two grooves, having a distance of 25 mm with the first mesh tube, were manufactured at the entrance of the copper tube. Moreover, two copper wires which other ends were connected to the first mesh tube were embedded in the grooves. Thus, the mesh tubes were fixed and immovable in R245fa flow direction. Fig. 3e shows the mesh tube, which had a length of 370 mm and outside diameter of 11.32 mm. The tube was made by the rolling stainless steel mesh screen. The mesh screen had the PPI (pores per inch) of 900 and mesh pore width of 15 μm. The SEM image of the mesh screen is shown in Fig. 3f.

The flow pattern in tubes is largely affected by the wettability and surface roughness of tube wall. Fig. 3g shows the SEM image of inside wall surface of the copper tube. We performed the high speed flow visualization of an R245fa liquid droplet spreading on the copper tube surface. The tube wall surface could be treated as a completely hydrophilic surface with the contact angle of 38.4° (see Fig. 3h). The surface roughness also was measured by a surface profiler (type Bruker Dektak XT). The measuring roughness is 0.191 μm (see Fig. 3i), indicating the copper tube surface is quite smooth which minimizes the flow pattern difference between glass tube and copper tube.

Table 1 summarized the major parameter ranges of this study: Nine inclination angles (0°, ± 5°, ± 10°, ± 15° and ± 30°) were tested, $\theta = 0°$, $\theta > 0°$ and $\theta < 0°$ represent the horizontal flow, inclined upflow and inclined downflow, respectively. The R245fa mass fluxes G_r and inlet vapor mass qualities x_{in} were at the range of 198.8–504.7 kg/m^2 s and 0.296–0.932, respectively. The cooling water inlet temperature $T_{c,in}$ was kept at 25.3 ± 0.5 °C. The mass flow rate of cooling water was maintained at about 1070 kg/h, corresponding to its Reynolds number of 4028. We note that the heat flux of the condenser is calculated based on the temperature difference of cooling water between inlet and outlet. During the experiments, the temperature difference of cooling

Table 1
Experimental running parameters.

Parameters	Range
Inclination angle, θ	−30° to 30°
Mass flux, G_r	198.8–504.7 kg/m^2 s
Inlet vapor temperature, $T_{r,in}$	63.1 ± 0.3 °C
Inlet vapor pressure, p_{in}	504.6 ± 5.0 kPa
Inlet vapor mass quality, x_{in}	0.296–0.932
Heat duties of test section, Q	7.5–14.9 kW
Heat flux on the inner side wall, q	33.78–67.2 kW/m^2
Cooling water mass flow rate, m_c	1069.4 ± 8.6 kg/h
Cooling water inlet temperature, $T_{c,in}$	25.3 ± 0.5 °C
Cooling water temperature difference, ΔT_c	7.7 °C–12.2 °C

Table 2
Major parameters, instruments, uncertainties and manufacturers.

Parameters	Instruments and uncertainties	Manufacturers
Fluid temperature	K-type jacket thermocouple, 0.2 °C	OMEGA Engineering Inc.
Wall temperature	K-type jacket thermocouple, 0.2 °C	OMEGA Engineering Inc.
Mass flow rate	DMF-1 mass flow meter, 0.1%	Beijing Sincerity Automatic Equipment Co., Ltd.
Pressure	Rosemount-3051 pressure transducer, 0.5%	Emerson Process Management Co., Ltd.
Voltage	GDU2-C55 DC voltage transmitter, 0.5%	Beijing Passion Technology Co., Ltd.
Current	HDIC-C21 DC current transmitter, 0.5%	Beijing Passion Technology Co., Ltd.

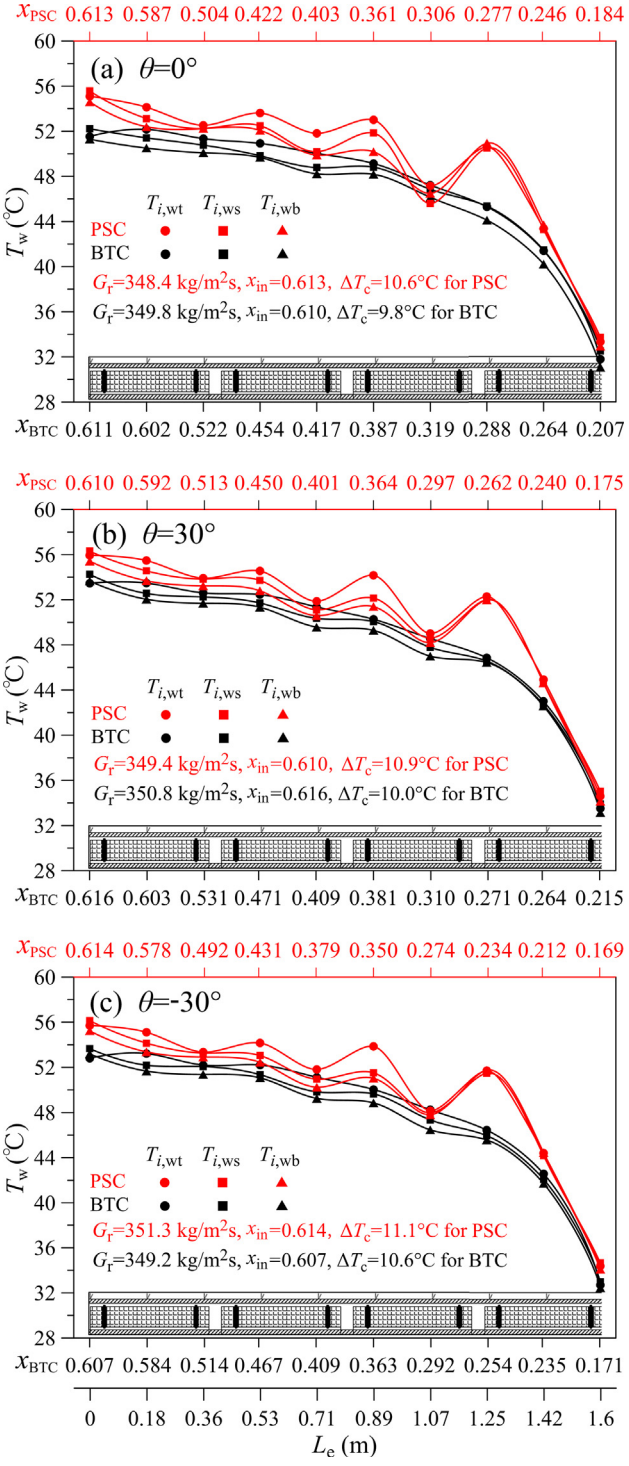

Fig. 4. Copper wall temperatures for PSC and BTC at three inclination angles.

water between inlet and outlet is controlled at the range of 7.7–12.2 °C. Increasing the cooling water flow rate will reduce the temperature difference between inlet and outlet, which tend to exaggerate the thermocouple measurement error. In order to obtain the reliable experimental results, the cooling water flow rate should not be too large.

3.3. Data reduction and uncertainty analysis

The condenser inlet enthalpy ($i_{r,in}$) and quality (x_{in}) were:

$$i_{r,in} = i_{eva,in} + \frac{UI\eta_{eva}}{m_r} \tag{7}$$

$$x_{in} = \frac{i_{r,in} - i_{l,in}}{i_{lg,in}} \tag{8}$$

where $i_{eva,in}$ is the R245fa enthalpy at the evaporator inlet, $i_{l,in}$ and $i_{lg,in}$ are the R245fa saturated liquid enthalpy and latent heat of evaporation based on the condenser inlet pressure, respectively.

Heat received by the cooling water in condenser was

$$Q = m_c C_{p,c}(T_{c,out} - T_{c,in}) \tag{9}$$

The modulated tubes with mesh tubes inserted in this study do not extend the condensation heat transfer area. To modulate flow patterns in tubes, the mesh tubes are suspended in the condenser tube. The mesh tube surface prevents R245fa vapor entering the mesh cylinder but captures liquid into the mesh cylinder, ensuring larger vapor void fractions near the copper tube wall. The condensation heat transfer area is the area of copper tube wall surface, which is not included the area of mesh tube surface. Thus, heat flux based on the inner copper tube wall surface was

$$q = \frac{Q}{3\pi d_i L_e} \tag{10}$$

where 3 represents the three copper tubes, L_e is the effective heat transfer length (L_e = 1.60 m). The outlet R245fa mixture enthalpy and quality were

$$i_{r,out} = i_{r,in} - \frac{Q}{m_r \eta_{con}} \tag{11}$$

$$x_{out} = \frac{i_{r,out} - i_{l,out}}{i_{lg,out}} \tag{12}$$

where $i_{l,out}$ and $i_{lg,out}$ are the R245fa saturated liquid enthalpy and latent heat of evaporation based on the condenser outlet pressure, respectively.

Heat transfer coefficient (h) is based on the average vapor mass quality, written as $x_{ave} = 0.5(x_{in} + x_{out})$. Thus, h was computed as [22,23]:

$$h = \frac{1}{\frac{1}{h_{to}} - \frac{d_i}{2k_w}\ln\left(\frac{d_o}{d_i}\right) - \frac{d_i}{d_o}\frac{1}{h_c}} \tag{13}$$

where k_w is the thermal conductivity of the copper tube. The total heat transfer coefficient h_{to} in Eq. (13) was

$$h_{to} = \frac{q}{LMTD} \tag{14}$$

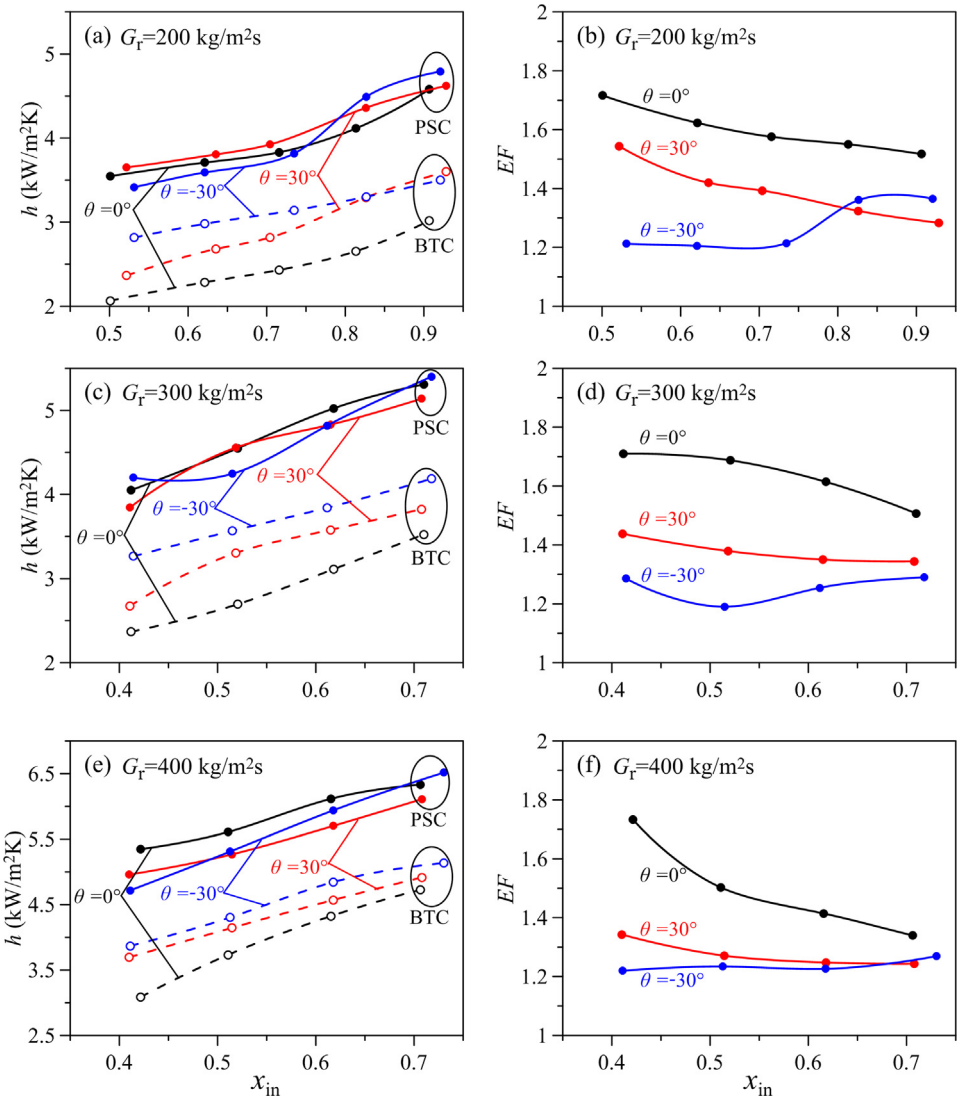

Fig. 5. Effects of inlet vapor mass qualities on condensation heat transfer coefficients and *EF* at three inclination angles.

where *LMTD* temperature difference was defined as

$$LMTD = \frac{(T_{r,in}-T_{c,out})-(T_{r,out}-T_{c,in})}{\ln\left(\frac{T_{r,in}-T_{c,out}}{T_{r,out}-T_{c,in}}\right)} \quad (15)$$

Heat transfer coefficient for cooling water was

$$h_c = \frac{qd_i}{d_o(T_{w,ave}-T_{c,ave})} \quad (16)$$

where $T_{w,ave}$ and $T_{c,ave}$ are the average temperatures of the tube wall and cooling water, which were

$$T_{w,ave} = \frac{1}{3n}\sum_{i=1}^{n}(T_{i,wt}+T_{i,ws}+T_{i,wb}), \quad T_{c,ave} = \frac{1}{3n}\sum_{i=1}^{n}(T_{i,cl}+T_{i,cr}+T_{i,cb}) \quad (17)$$

where *i* is the cross section number, *n* equals to 10 here. Total pressure drop in the condenser was$\Delta P = P_{r,in}-P_{r,out}$.

The heat transfer enhancement ratio (*EF*) was defined as [17]:

$$EF = \frac{h_{PSC}}{h_{BTC}} \quad (18)$$

where h_{PSC} and h_{BTC} were the heat transfer coefficients of the phase separation condenser and the bare tube condenser at the same inclination angle.

To evaluate heat transfer enhancement at the cost of pressure drop, the performance evaluation parameter (*PEC*) was defined as [17]:

$$PEC = \frac{h_{PSC}/h_{BTC}}{(\Delta P_{PSC,f}/\Delta P_{BTC,f})^{1/6}} \quad (19)$$

where ΔP_f was the two-phase friction pressure drop, which was subtracted the acceleration pressure drop ΔP_a and gravity pressure drop ΔP_g from the measured total pressure drop ΔP [23]. Fan et al. [28] concluded that the power exponent of pressure drops in *PEC* is at the range of 0–1/3 based on identical pumping power. For single-phase heat transfer enhancement, 1/3 is usually used in the power exponent. But for two-phase heat transfer enhancement, 1/6 is widely used in the published papers [29,30].

High quality sensors and instruments were used in our study. Table 2 summarized the uncertainties of the instruments. Both AC voltage and current had the uncertainties of 0.2%. Industrial Personal Computer (IPC) with 100 signal processing channels was used as the data acquisition system. Furthermore, the heat transfer coefficient (*h*), enhanced heat transfer ratio (*EF*) and (*PEC*) values were determined by directly measured parameters. The uncertainties of these parameters were evaluated on the basis of the error transmission theory [31]. In this study, *h*, *EF* and *PEC* had the accuracies of 5.47%, 8.63% and 9.13%, respectively.

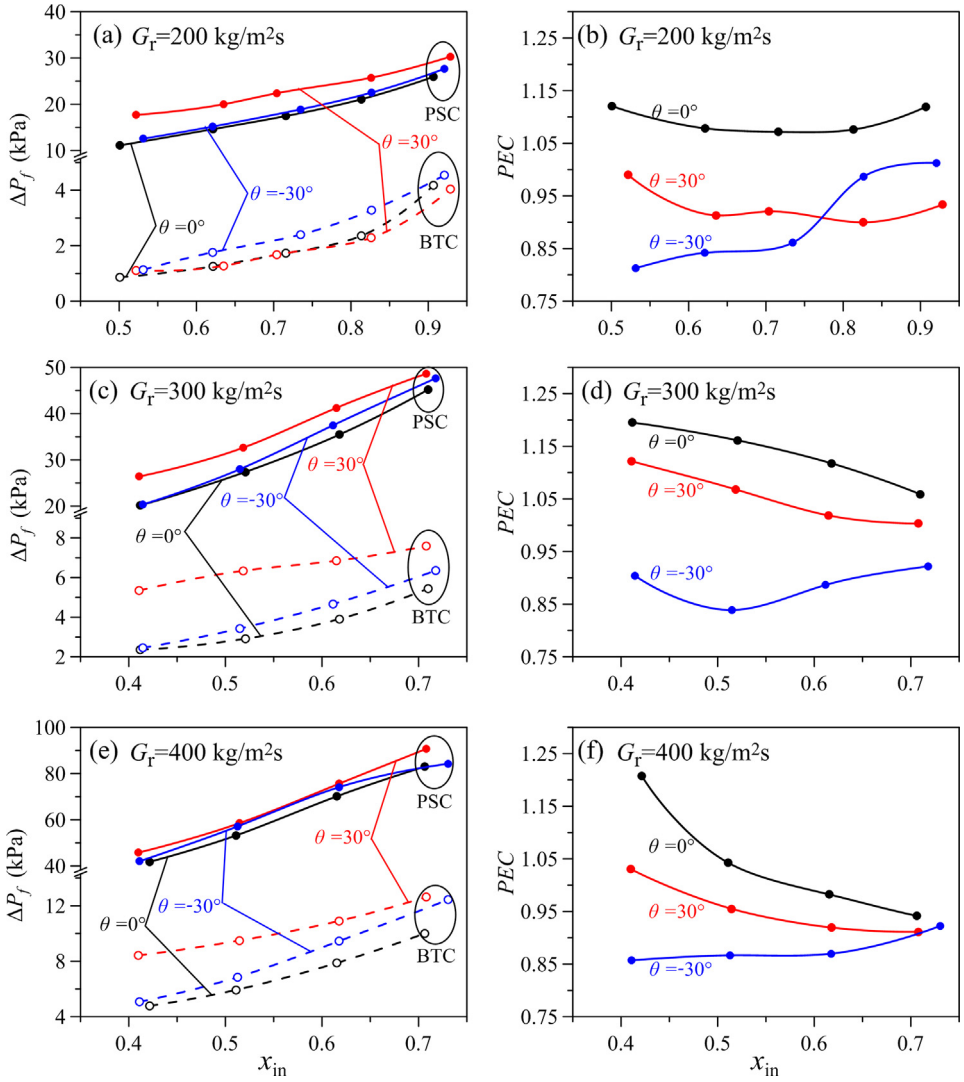

Fig. 6. Effects of inlet vapor mass qualities on friction pressure drops and *PEC* at three inclination angles.

3.4. Calibration experiment

R245fa enthalpy under its two-phase state cannot be only determined by the measured temperature and the specific heat of R245fa is relatively small. Thus, in order to get similar tube wall temperature condition as that for R245fa two-phase flow, calibration experiments using water instead of R245fa as the working fluid was performed to obtain the efficiencies of evaporator and condenser. Bare tube condenser (BTC) was used as the test condenser in the calibration experiment.

The evaporator thermal efficiency was

$$\eta_{eva} = \frac{m_w C_{p,w}(T_{(w,eva),out} - T_{(w,eva),in})}{UI} \quad (20)$$

where m_w is the water mass flow rate, $C_{p,w}$ is the water specific heat, $T_{(w,eva),out}$ and $T_{(w,eva),in}$ are the evaporator outlet and inlet water temperatures, respectively, U and I are the voltage and current of the AC electrical power, respectively. The measured evaporator thermal efficiency was about 0.91 (average value).

Similarly, the test condenser thermal efficiency was

$$\eta_{con} = \frac{m_{w,s} C_{p,(w,s)}(T_{(w,s),out} - T_{(w,s),in})}{m_{w,t} C_{p,(w,t)}(T_{(w,t),out} - T_{(w,t),in})} \quad (21)$$

where the subscripts (w,t) and (w,s) mean the water in tube side and shell side of BTC, respectively. The measured average condenser thermal efficiency η_{con} reached about 0.98.

The heat transfer and pressure drop calibration experiments directly used R245fa as the working fluid. The calibration experiment was conducted at horizontal BTC in our previous study [22]. The measured condensation heat transfer coefficient well matched Dobson & Chato [32] correlation. The relative difference was less than −13.56%, which is acceptable for two-phase condensation heat transfer. The measured two-phase friction pressure drops were well matched the correlation of Laohalertdecha & Wongwises [33], with the relative difference less than −11.63%. Besides, calibration experiments were also performed when the measured copper tube was at the top location and at the lower position. It was less than −4.87% for the relative difference of condensation heat transfer coefficient calculated according to the measured data, indicating that the difference of the flow rate is little in the three tubes. Thus, our experimental results were believable for condensation of shell-tube condenser.

4. Results and discussion

4.1. Heat transfer characteristics

Fig. 4 shows measured copper wall temperatures for PSC and BTC at three inclination angles ($\theta = 0°$, $\theta = 30°$ and $\theta = -30°$). The R245fa

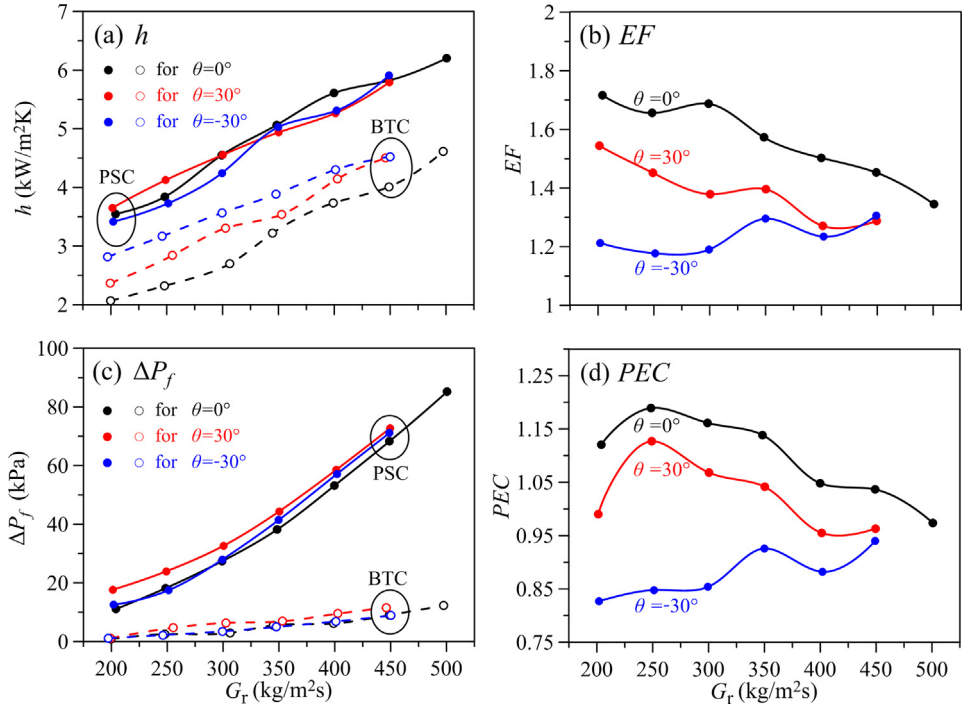

Fig. 7. Effects of mass fluxes on enhancement heat transfer at three inclination angles and $x_{in} \approx 0.5$.

mass fluxes G_r and condenser inlet vapor mass qualities x_{in} were about 350 kg/m^2 s and 0.6, respectively. Wall temperatures for BTC decrease along the length of copper tube, but they fluctuate at the end of each inserted mesh tubes for PSC. R245fa vapor and liquid were mix at the end of each inserted mesh tubes, the vapor void fractions near the tube wall were decreased. However, the vapor void fractions were increased at the top of next mesh tube. That is mechanism for wall temperatures fluctuation at the end of each inserted mesh tubes. The vapor mass qualities were also decreased along the length of copper tube, so the vapor void fractions near the tube wall at the end of next mesh tube were greatly decreased and the wall temperatures fluctuation will become larger along the flow direction. On the other hand, the copper wall temperatures for PSC were higher than that in BTC, indicating the little temperature difference between R245fa mixture and copper tube wall. Thus, condensation heat transfer coefficients for PSC became larger. Higher wall temperatures increased the temperature difference between the copper tube wall and cooling water, yielding the larger heat transfer rate. ΔT_c refers to the temperature difference between cooling water outlet and inlet and it is proportionate to heat transfer rate. The increased heat transfer rates were 8.26%, 9.00% and 4.71% for three inclination angles, respectively. Alternatively, wall temperatures and ΔT_c for BTC at inclined angles were slightly larger than that in the horizontal position, indicating the positive effect of inclined angles on the condensation heat transfer. However, inclined angles had relatively small influence on the heat transfer enhancement for PSC.

Fig. 5 shows the results of condensation heat transfer coefficients and heat transfer enhancement ratios. Both tests of BTC and PSC were performed at the same x_{in}. Condensation heat transfer coefficients are quasi-linearly increased with increasing inlet vapor mass qualities. With the increasing inlet vapor mass qualities, the velocities both of liquid and vapor flows were increased, whereas the liquid heights were decreased. Hence, condensation heat transfer coefficients were increased. PSC had much larger condensation heat transfer coefficients than BTC. Inclination angles had pronounced effects on h for BTC, both inclined upflow and downflow could enhance condensation heat transfer. For BTC, $\theta = -30^\circ$ had the largest heat transfer coefficients, then $\theta = 30^\circ$, and $\theta = 0^\circ$ is the worst. But for PSC, horizontal position had the best heat transfer performance among three inclination angles. The heat transfer enhancement ratio *EF* was defined as the h for PSC divided by that for BTC at the same inclination angle. *EF* values were decreased with the increase of x_{in}, at the range of 1.21–1.72. *EF* values at $\theta = 0^\circ$ were much larger than that at $\theta = \pm 30^\circ$, indicating PSC in the horizontal position enhanced the heat transfer greatly. The 1.72 maximum *EF* occurred at $\theta = 0^\circ$, $G_r = 200$ kg/m^2 s and $x_{in} = 0.501$. Xie et al. [17] proposed the maximum *EF* up to 2.0 by using R123 as working fluid. We note that the condensation heat transfer is very complicated, which is affected by many parameters. First, the working fluid is different and the pressure at the test section inlet was maintained at about 505 kPa in this study but it only about 255 kPa in Xie' study. Moreover, Xie employed the two layers screen surface mesh tube but the single layer screen surface mesh tube was used in this paper. Even though the higher *EF* can be achieve as the two layers screen surface mesh tube was used, the one-quarter of *PEC* values is less than one, indicating more cost of pressure drop. To balance the heat transfer enhancement and pressure drop cost, the single layer mesh screen surface is more suitable for modulated tube with mesh tube inserted. The *PEC* values in horizontal position larger than 1 is totally achieved in our study which is attractive for users and we will discuss in the next section.

Fig. 6 shows the friction pressure drops ΔP_f and performance evaluation parameters *PEC* versus x_{in}. The friction pressure drops also increased with the increasing x_{in}. Due to the flow resistance in the mesh surfaces, the friction pressure drop in PSC increased at a much steeper rate with x_{in} than BTC. It can be observed that friction pressure drops in the horizontal position is the minimum among three inclination angles. The maximum ΔP_f always occurred at $\theta = 30^\circ$. Heat transfer device is recommended for applications if *PEC* is larger than 1. The *PEC* values were decreased with the increasing x_{in} for $\theta = 0^\circ$ and 30°, but they were increased with the increasing x_{in} for $\theta = -30^\circ$. $\theta = 0^\circ$ had the largest *PEC*, then $\theta = 30^\circ$, and $\theta = -30^\circ$ was the worst. Because of the comparatively larger *EF* and lower ΔP_f, PSC in the horizontal position had *PEC* larger than 1. The maximum *PEC* is 1.21, which occurred at $G_r = 400$ kg/m^2 s and $x_{in} = 0.404$. However, *PEC* values were mostly less than 1 if PSC was installed at $\theta = \pm 30^\circ$.

Fig. 7 shows the effects of mass fluxes on the condensation heat transfer coefficients, the heat transfer enhancement ratios, the measured friction pressure drops and performance evaluation parameters

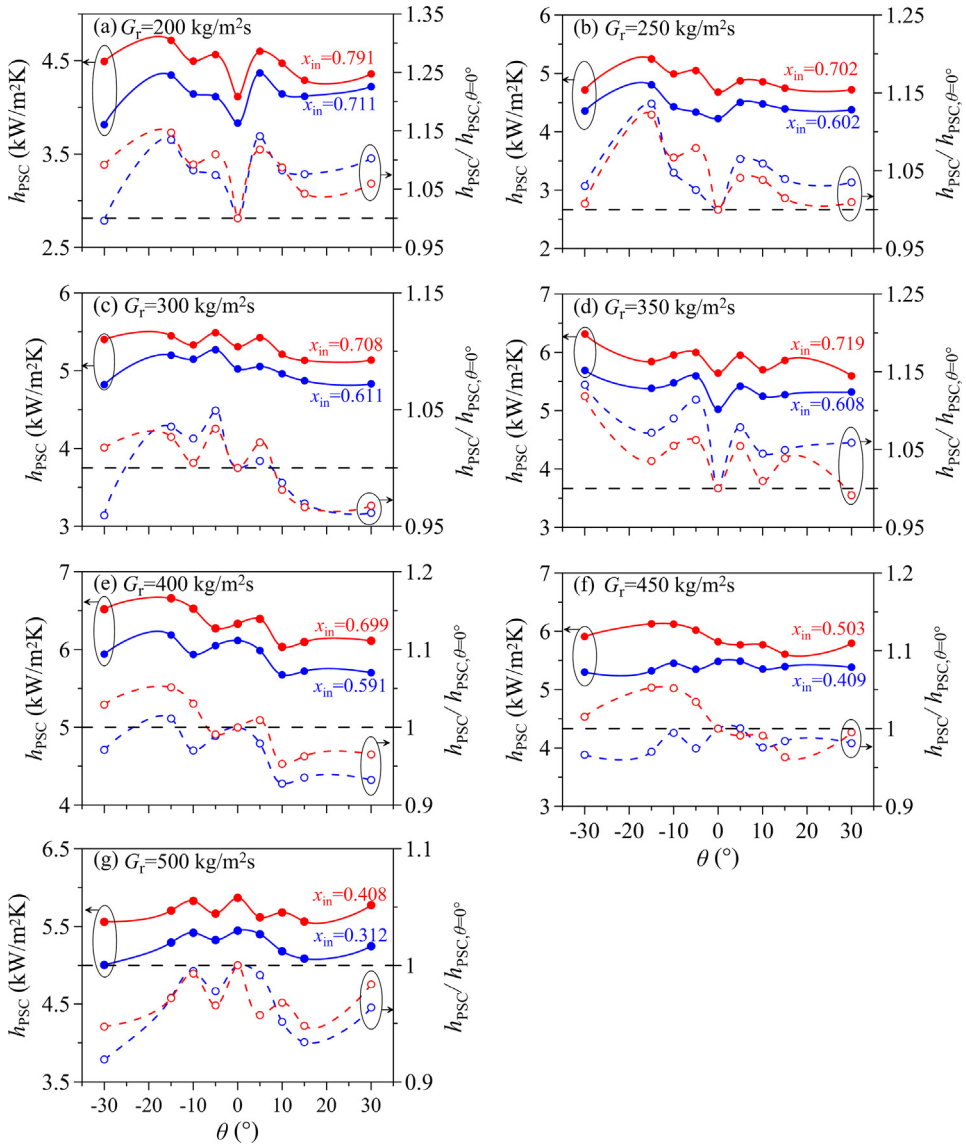

Fig. 8. Effects of inclination angles on condensation heat transfer coefficients of PSC.

versus mass fluxes at three inclination angles and $x_{in} \approx 0.5$. With the increasing mass fluxes, the flow velocities and shear stress at the vapor-liquid interface were increased, indicating the higher h and ΔP_f. $\theta = 0°$ always had the maximum h and minimum ΔP_f among three inclination angles for PSC, whereas a contrary behavior was observed for BTC. The *EF* and *PEC* values were also decreased quasi-linearly with the increasing G_r at $\theta = 0°$ and 30°, but they were increased with the increasing G_r at $\theta = -30°$. $\theta = 0°$ had the largest *EF* and *PEC* values among three inclination angles, then $\theta = 30°$, and $\theta = -30°$ was the worst.

4.2. Effect of inclination angles

Fig. 8 identifies the effects of inclination angles on the condensation heat transfer coefficients for PSC at seven mass fluxes and various inlet vapor mass qualities. The parameter $h_{PSC}/h_{PSC,\theta=0}$, was defined as the condensation heat transfer coefficients of PSC at corresponding inclination angle divided by that in the horizontal position, which was used to clearly see the effects of inclination angles. Generally speaking, $h_{PSC}/h_{PSC,\theta=0}$ had a decreasing trend with the increasing inclination angles in the range of $-30°$ to 30° at $G_r < 500\ kg/m^2s$. The $h_{PSC}/h_{PSC,\theta=0}$ values also exhibited the non-monotonic behavior against the inclination angles. For the inclined upward flow with $0° < \theta < 30°$, the maximum $h_{PSC}/h_{PSC,\theta=0}$ always occurred at about $\theta = 5°$. For the inclined downward flow with $-30° < \theta < 0°$, the maximum $h_{PSC}/h_{PSC,\theta=0}$ always occurred at about $\theta = -15°$. However, the larger condensation heat transfer coefficients occurred at the $\theta = 0°$ and $G_r = 500\ kg/m^2s$.

Fig. 9 shows the enhancement heat transfer evaluation factors *EF* and *PEC* versus θ at the same mass fluxes and inlet vapor mass qualities in Fig. 8. Both *EF* and *PEC* values exhibited the approximate parabola relationship against the inclination angles in the range of $-30°$ to 30°. The maximum *EF* and *PEC* occurred at $\theta = 0°$, corresponding to the horizontal flow. Both inclined upflow and downflow weaken heat transfer enhancement of PSC. To reach better condensation heat transfer performance, the PSC heat exchanger should be operated in the horizontal position.

4.3. Flow pattern observations in the bare tube

In order to understand the mechanisms of the phase change heat transfer in the tube with mesh tube inserted, flow patterns in the bare tube were observed through a smooth quartz glass tube having the same inner diameter of the copper tube. The flow pattern in the mesh

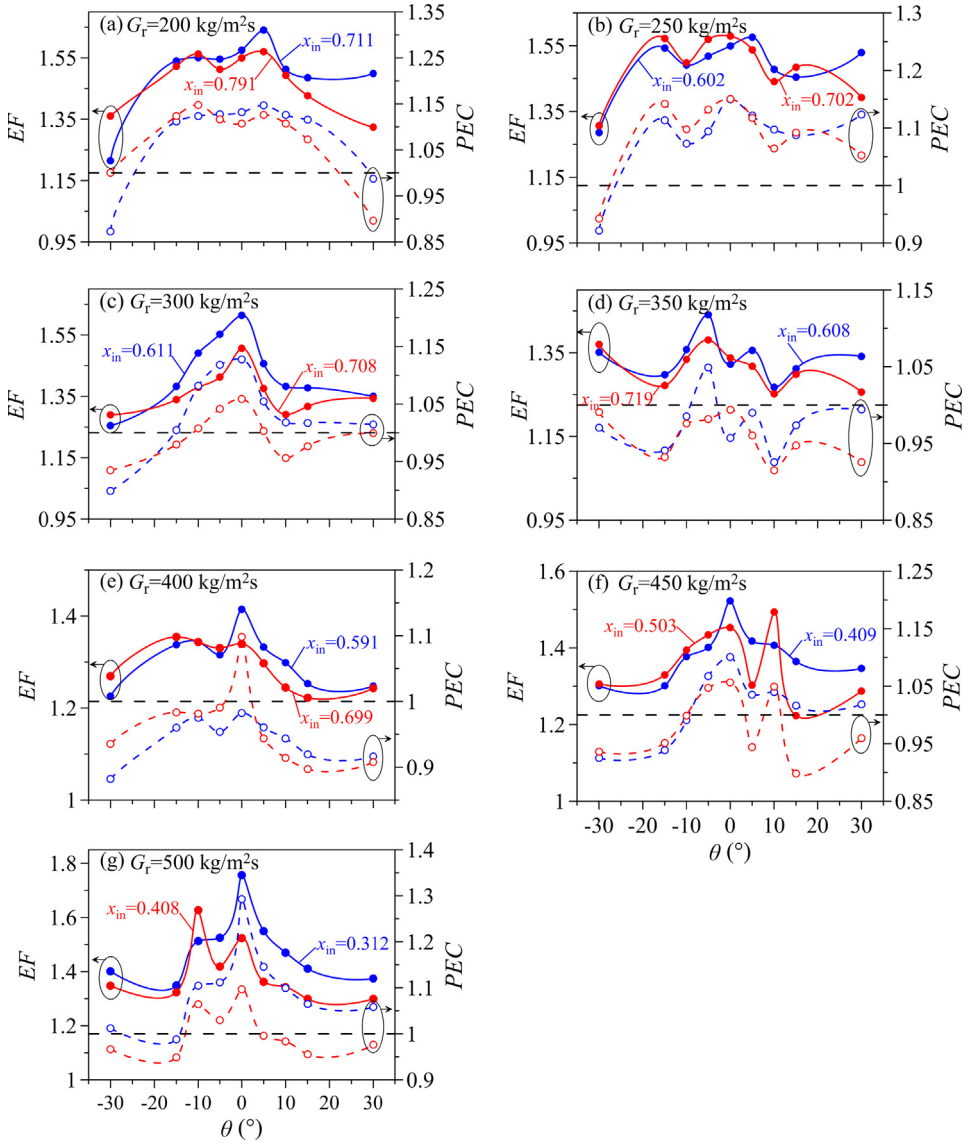

Fig. 9. Effects of inclination angles on enhancement heat transfer evaluation factors *EF* and *PEC*.

inserted tube is different from that of in the bare tube, which will be discussed in the Section 4.4. Fig. 10 shows the flow pattern maps at three inclination angles of $\theta = 0^\circ$, $-15^\circ$and 15°. Flow pattern images were shown in the right column. Four flow patterns were observed, including the annular flow (A), intermittent flow (I), stratified-wavy flow (SW), and stratified-smooth flow (SS). These flow pattern definitions can be found in Ref [21]. Because the relatively lower surface tension force of R245fa and the larger tube diameter, the flow patterns are mainly dominated by the gravity force and inertia force. The positive effect of gravity force and negative effect of buoyancy force for inclined downflow could accelerate the liquid flow and decelerate the vapor flow. The liquid heights were decreased and the flow became more stable, yielding the smaller region of SW flow and the appearance of SS flow. However, the negative effect of gravity force and positive effect of buoyancy force for inclined upflow could accelerate the vapor flow and decelerate the liquid flow. The shear stress on the vapor-liquid interface is increased, yielding the more unstable interface. Thus, the SS flow was not observed in the inclined upflow and the flow was more unstable. The relatively stronger interface wave and lower liquid heights were the mechanisms for heat transfer enhancement in the bare tube at different inclination angles.

Fig. 11 shows the dynamic interfaces of three cases at different inclination angles of 0° and $\pm 15^\circ$ with the same mass flux of $G_r = 196.8\,kg/m^2\,s$ and $x = 0.096$. We can clearly see that more stable flow can be obtained at $\theta = -15^\circ$, but the stronger vapor-liquid interface wave exists at $\theta = 15^\circ$. Meanwhile, compared to $\theta = 15^\circ$, $\theta = 0^\circ$ has a higher liquid flow speed.

4.4. Enhanced heat transfer mechanism for specific flow patterns and inclination angles

The annular flow contains a vapor core and a liquid film on the tube wall. Liquid droplets, which leave from the film, are entrained in the vapor core. Fig. 12 shows the spreading process of an R245fa droplet on mesh surface. Initially, a 1.36 mm diameter R245fa droplet is on the mesh surface at $t = 0$. Then the droplet quickly spreads and penetrates the mesh surface. Finally, the droplet thoroughly spreads on mesh surface with a wetting area of 46.4 mm^2 at $t = 100$ ms. Thus, the liquid droplets in annular flow were captured by the mesh surface. The liquid film on the tube wall becomes thinner, which would enhance the heat transfer.

Fig. 13 shows the stratified flow pattern modulation. Fig. 13a demonstrates the modulation photo at $G_r = 198.4\,kg/m^2\,s$, $x = 0.102$, and $\theta = 0^\circ$. Cross sections A-A and B-B are in the bare tube section and

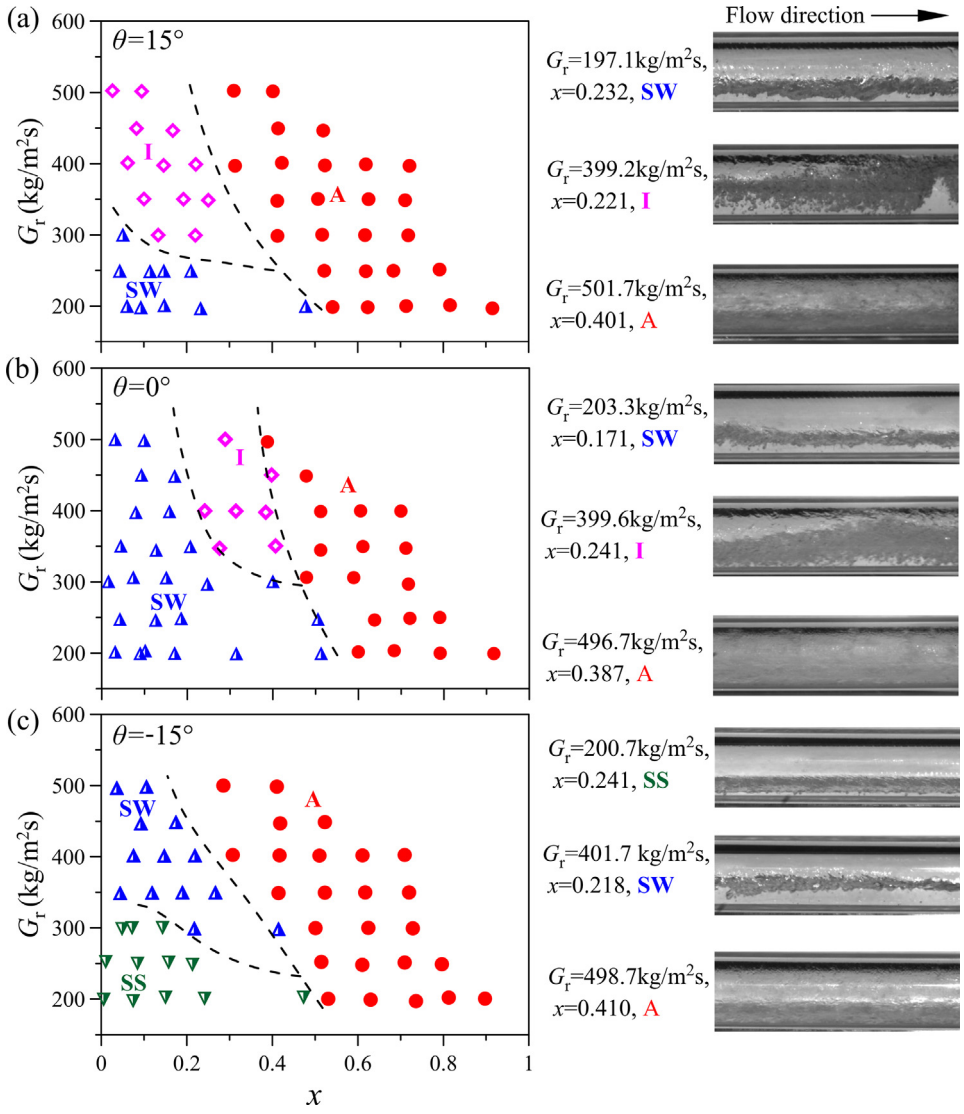

Fig. 10. Flow pattern maps in bare tube at three inclination angles (A: annular flow, I: intermittent flow, SW: stratified-wavy flow, SS: stratified-smooth flow).

modulated flow section, respectively. The heat transfer enhancement is related to the phase distribution in tubes. The heat transfer rate is directly related to the tube surface area exposed in vapor:

$$q_t = \alpha S_g \Delta T \tag{22}$$

where q_t is the heat transfer rate in the tube along a unit flow length, α is the thin film condensation heat transfer coefficient, ΔT is the temperature difference between tube wall and R245fa saturation temperature. S_g is the tube circumference length exposed in vapor, which is

$$S_g = \pi d_i - d_i \cdot \arccos\left(1-\frac{2h_l}{d_i}\right) \tag{23}$$

where h_l is the liquid height. The *EF* can also be deduced as:

$$EF = \frac{S_{g,B}}{S_{g,A}} = 1 + \frac{\arccos\left(1-\frac{2h_{l,A}}{d_i}\right) - \arccos\left(1-\frac{2h_{l,B}}{d_i}\right)}{\pi - \arccos\left(1-\frac{2h_{l,A}}{d_i}\right)} \tag{24}$$

Comparing the two cross sections in Fig. 13b, the h_l is 4.82 mm at cross sections A-A but it reduces to just 1.28 mm at cross sections B-B. The *EF* value reaches 1.274, indicating heat transfer improvement of 27.4% can be obtained at similar running condition.

Fig. 14 shows pressure balance analysis for copper tube with mesh tube inserted at inclination angles. $P_{an,1}$ and $P_{co,1}$ are the upstream pressures in the annular region and core region, respectively. $P_{an,2}$ and $P_{co,2}$ are the exit pressures in the annular region and core region, respectively. Due to the R245fa fluid flows, from the annular region and core region, are mixed together at the mesh tube exit, it is reasonable to assume $P_{an,2} \approx P_{co,2}$. For two-phase flow in the annular region, $P_{an,1}$ -$P_{an,2}$ is

$$P_{an,1} - P_{an,2} = \Delta P_{f,an} \phi_l^2 + \rho_m g L \sin(\theta) \tag{25}$$

where $\Delta P_{f,an}$ is the frictional pressure drop if liquid flows alone, ϕ_l is the two-phase multiplier ratio, which was correlated based on the Chisholm method [34]. ρ_m is the two-phase mixture density in the annular region, and L is the length between the cross sections 1 and 2.

For liquid flow in the core region, $P_{co,1}$–$P_{co,2}$ is

$$P_{co,1} - P_{co,2} = \Delta P_{f,co} + \rho_l g L \sin(\theta) \tag{26}$$

where $\Delta P_{f,co}$ and ρ_l are the liquid frictional pressure drop and density in the core region.

Combining Eq. (25) and Eq. (26), $P_{an,1}$ –$P_{co,1}$ can be expressed as

$$P_{an,1} - P_{co,1} \approx \Delta P_{f,an} \phi_l^2 - \Delta P_{f,co} + (\rho_m - \rho_l) g L \sin(\theta) \tag{27}$$

$P_{an,1}$–$P_{co,1}$ is the driving force for R245fa liquid flow towards the mesh cylinder, which is the difference of two-phase pressure drop in annular region and liquid pressure drop in the core region. Form Eq.

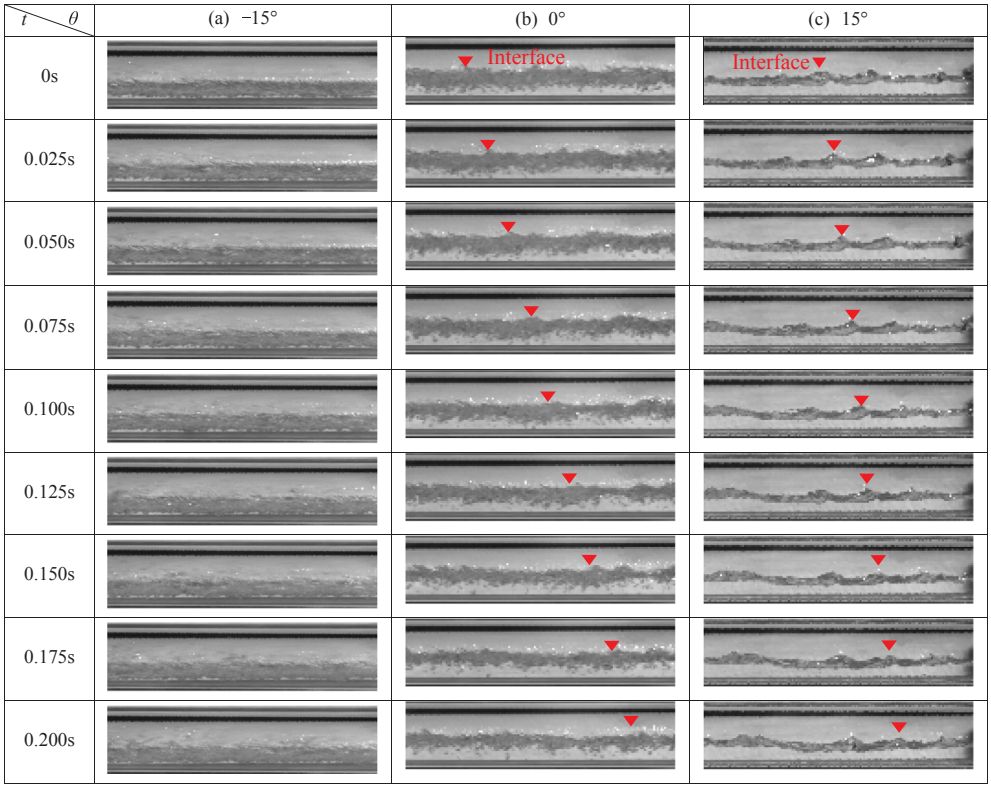

Fig. 11. Dynamic interfaces at the inclination angles of 0° and ± 15° at G_r = 196.8 kg/m^{2}s and x = 0.096 (the flow was from left to right).

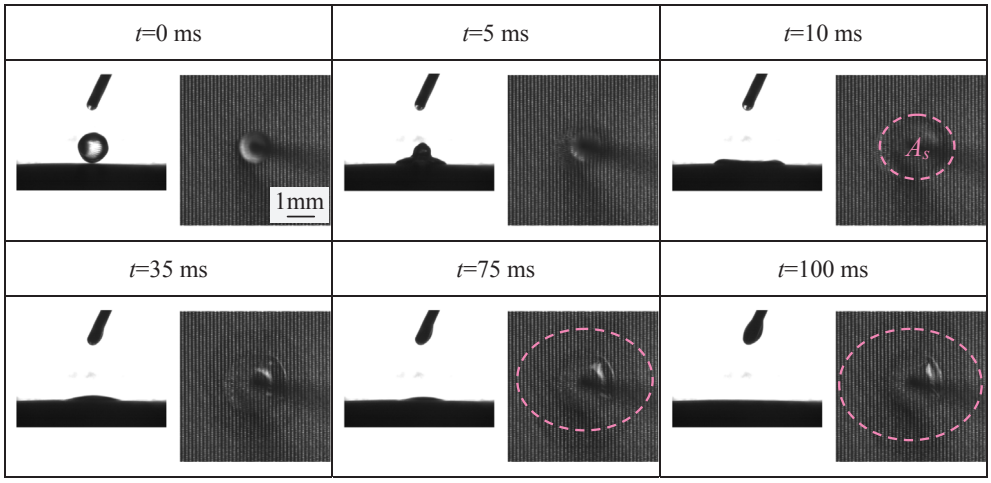

Fig. 12. High-speed observation of an R245fa liquid droplet spreading process on the mesh screen surface.

(27), we can clearly see that gravity force plays an important role to influence the driving force. Because the liquid density is larger than that of two-phase mixture, gravity force has the positive effect on the driving force for liquid flow towards the core region for inclined downflow. The inclined downflow had the largest driving force, then the horizontal flow, and the inclined upflow was the worst. That is the reason of h_{PSC} had a decreasing trend with the increasing inclination angles in the range of −30° to 30°.

Fig. 15 shows the stratified flow pattern modulation at three inclination angles of θ = 15°, 0° and −15°. The R245fa mass fluxes G_r and vapor mass qualities x were about 300.4 kg/m^{2}s and 0.051, respectively. Cross sections A-A and B-B were flow sections in the bare tube and inserted mesh tube, respectively. The average h_l/d_i values at cross sections A-A are decreased from 0.343 to 0.207, showing the increased liquid heights when the inclination angles are increased. On the other hand, we can clearly see that it exist more unstable vapor-liquid interface for inclined upflow. The inclined downflow also had the minimum average h_l/d_i value at cross sections A-A and B-B. The minimum average liquid height yields the smallest contact area between the liquid and mesh surface. However, liquid height difference between inclined upflow and horizontal flow was not noticeable at cross section B-B.

There is a pressure difference between two-phase flow in annular region and liquid flow in core region to drive liquid flow towards the core region, which could reduce liquid film thickness on the tube bottom. This is the mechanism to enhance heat transfer performance of PSC. The driving force was decreased with the increasing inclination angles. The heat transfer enhancement ratios were balanced by the driving force and contact area between the liquid and mesh surface. The best heat transfer enhancement performance occurred at the horizontal

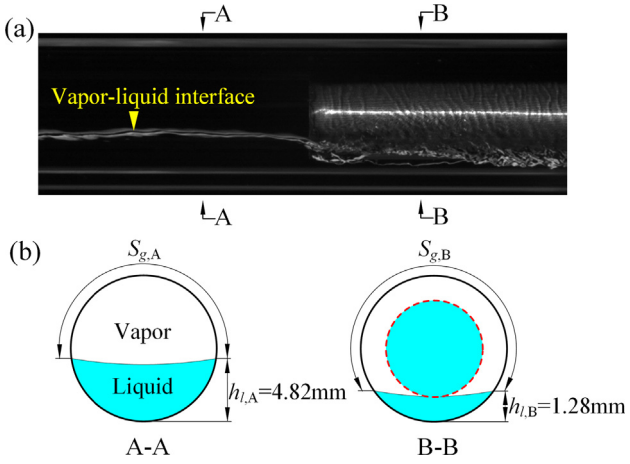

Fig. 13. Stratified flow pattern modulation for the condenser tube with mesh tube inserted.

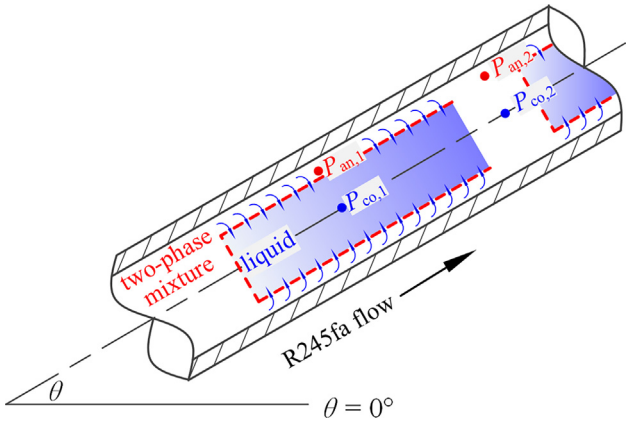

Fig. 14. Pressure balance analysis for copper tube with mesh tube inserted at inclination angles.

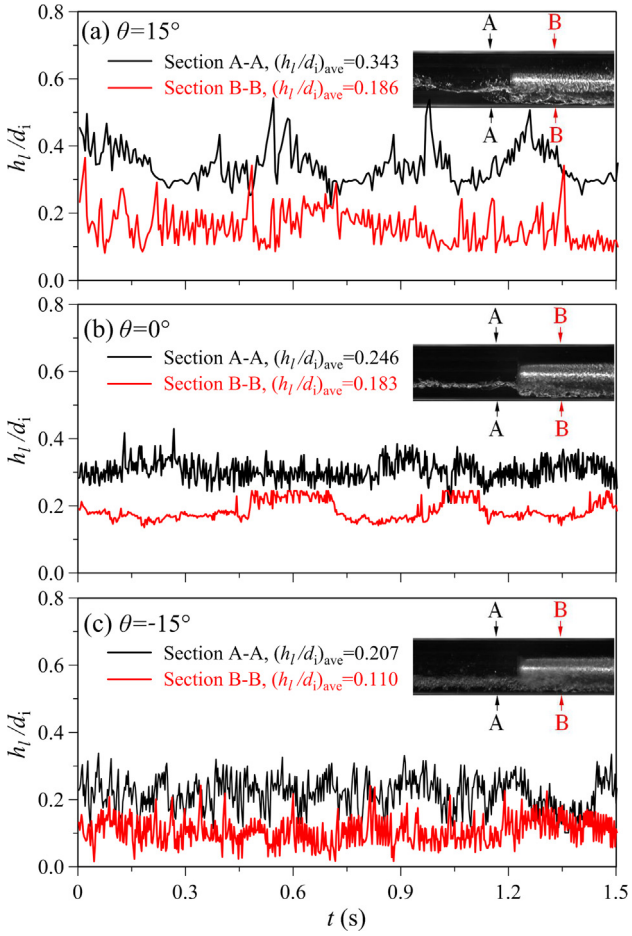

Fig. 15. Stratified flow pattern modulation at three different inclination angles and G_r = 300.4 kg/m^2 s, x = 0. 051.

flow. The reasons can be explained as follows: for inclined upflow, the driving force was relatively small, which had a negative effect on the heat transfer enhancement of PSC, while inclined downflow had the smallest contact area between the liquid and mesh surface. The best match between the driving force and contact area exists in the horizontal position, thus at this direction the heat transfer performance is enhanced largely.

5. Conclusions

The major results obtained from this study are summarized as following:

- Over the whole experiment data ranges, PSC obviously enhances condensation heat transfer, compared with BTC. Even though PSC increases frictional pressure drops, *PEC* is always larger than 1.0 in horizontal position which attracts users. *EF* and *PEC* are decreased with increase of vapor mass qualities and mass fluxes.
- BTC reaches the largest and smallest heat transfer coefficients for inclined downflow and horizontal flow, respectively. Compared with BTC, the sensitivity of the effect of inclined angles on heat transfer coefficients is weakened for PSC. PSC shows a slight decrease trend of heat transfer coefficients with increase of inclination angles in the range from $-30°$ to 30° having $G_r < 500\,kg/m^2 s$. At horizontal flow, PSC holds the maximum $EF = 1.72$ and $PEC = 1.21$.
- The pressure difference between annular region and core region drives liquid flow towards core region, reducing liquid film thickness on tube bottom and increasing vapor void fractions near tube wall, which are the major heat transfer enhancement mechanism for PSC.
- For PSC, both inclined upflow and downflow weaken the heat transfer enhancement. The pressure difference of annular region and core region and liquid-mesh contact area are the two main factors to influence heat transfer. If one increases inclination angles from $-30°$ to 30°, the pressure difference between annular region and core region is decreased, but the liquid-mesh contact area is increased. The horizontal position behaves an optimal match among the driving pressure difference and the liquid-mesh contact area, resulting in the maximum heat transfer enhancement ratios at such position.

6. Conflict of interest

The authors declare that there are no conflicts of interest.

Acknowledgements

This work was supported by Natural Science Foundation of China (51436004 and 51676071).

References

[1] K. Rahbar, S. Mahmoud, R.K. Al-Dadah, N. Moazami, S.A. Mirhadizadeh, Review of organic Rankine cycle for small-scale applications, Energy Convers. Manage. 134 (2017) 135–155.

[2] A. Panesar, R. Morgan, D. Kennaird, Organic Rankine cycle thermal architecture-from concept to demonstration, Appl. Therm. Eng. 126 (2017) 419–428.
[3] V. Chintala, S. Kumar, J.K. Pandey, A technical review on waste heat recovery from compression ignition engines using organic Rankine cycle, Renew. Sustain. Energy Rev. 81 (2018) 493–509.
[4] J. Bao, L. Zhao, A review of working fluid and expander selections for organic Rankine cycle, Renew. Sustain. Energy Rev. 24 (2013) 325–342.
[5] W.L. Cheng, H. Chen, S. Yuan, Q. Zhong, Y.F. Fan, Experimental study on heat transfer characteristics of R134a flow boiling in "Ω"-shaped grooved tube with different flow directions, Int. J. Heat Mass Transfer 108 (2017) 988–997.
[6] G.X. Liu, Y.J. Zhang, S.Z. Jiang, J.W. Liu, H.P. Gyimah, H.P. Luo, Investigation of pulse electrochemical sawing machining of micro-inner annular groove on metallic tube, Int. J. Mach. Tool Manu. 102 (2016) 22–34.
[7] M. Dastmalch, A. Arefmanesh, G.A. Sheikhzadeh, Numerical investigation of heat transfer and pressure drop of heat transfer oil in smooth and micro-finned tubes, Int. J. Therm. Sci. 121 (2017) 294–304.
[8] C.M. Yang, P. Hrnjak, Effect of straight micro fins on heat transfer and pressure drop of R410A during evaporation in round tubes, Int. J. Heat Mass Transfer 117 (2018) 924–939.
[9] W. Wang, Y.N. Zhang, B.X. Li, Y.J. Li, Numerical investigation of tube-side fully developed turbulent flow and heat transfer in outward corrugated tubes, Int. J. Heat Mass Transfer 116 (2018) 115–126.
[10] M. Sun, M. Zeng, Investigation on turbulent flow and heat transfer characteristics and technical economy of corrugated tube, Appl. Therm. Eng. 129 (2018) 1–11.
[11] T. Välikangas, S. Singh, K. Sørensen, T. Condra, Fin-and-tube heat exchanger enhancement with a combined herringbone and vortex generator design, Int. J. Heat Mass Transfer 118 (2018) 602–616.
[12] H.X. Chen, J.L. Xu, Z.J. Li, F. Xing, J. Xie, Stratified two-phase flow pattern modulation in a horizontal tube by the mesh pore cylinder surface, Appl. Energy 112 (2013) 1283–1290.
[13] H.X. Chen, J.L. Xu, Z.J. Li, F. Xing, J. Xie, W. Wang, W. Zhang, Flow pattern modulation in a horizontal tube by the passive phase separation concept, Int. J. Multiphas. Flow 45 (2012) 12–23.
[14] D.L. Sun, J.L. Xu, Q.C. Chen, Z. Cao, Numerical study of flow pattern modulation in a vertical phase separation condenser tube, Chinese Sci. Bull. 58 (2013) 1592–1598.
[15] D.L. Sun, J.L. Xu, Q.C. Chen, Y.Y. Yan, Modulated flow pattern in a condenser tube with two-phase flow interacting with mesh screen surface at micro-gravity, Int. J. Multiphas. Flow 69 (2015) 54–62.
[16] F. Xing, J. Xie, J.L. Xu, Modulated heat transfer tube with mesh cylinder inserted, Int. Commun. Heat Mass 56 (2014) 15–24.
[17] J. Xie, J.L. Xu, F. Xing, Z.X. Wang, H. Liu, The phase separation concept condensation heat transfer in horizontal tubes for low-grade energy utilization, Energy 69 (2014) 787–800.
[18] S. Lips, J.P. Meyer, Stratified flow model for convective condensation in an inclined tube, Int. J. Heat. Fluid. Flow 36 (2012) 83–91.
[19] T. Nitheanandan, H.M. Soliman, Influence of tube inclination on the flow regime boundaries of condensing steam, Can. J. Chem. Eng. 71 (1996) 35–41.
[20] S.G. Mohseni, M.A. Akhavan-Behabadi, M. Saeedinia, Flow pattern visualization and heat transfer characteristics of R-134a during condensation inside a smooth tube with different tube inclinations, Int. J. Heat Mass Transfer 60 (2013) 598–602.
[21] F. Xing, J.L. Xu, J. Xie, H. Liu, Z.X. Wang, X.L. Ma, Froude number dominates condensation heat transfer of R245fa in tubes: effect of inclination angles, Int. J. Multiphas. Flow 71 (2015) 98–115.
[22] S. Cao, J.L. Xu, Y.Z. Li, Y.Y. Yan, Condensation heat transfer of R245fa in a shell-tube heat exchanger at slightly inclined angles, Int. J. Therm. Sci. 115 (2017) 197–209.
[23] J. Xie, J.L. Xu, Y. Cheng, F. Xing, X.T. He, Condensation heat transfer of R245fa in tubes with and without lyophilic porous-membrane-tube insert, Int. J. Heat Mass Transfer 88 (2015) 261–275.
[24] G.B. Abadi, C. Moon, K.C. Kim, Effect of gravity vector on flow boiling heat transfer, flow pattern map, and pressure drop of R245fa refrigerant in mini tubes, Int. J. Multiphas. Flow 83 (2016) 202–216.
[25] J.L. Xu, X.M. Zhang, Start-up and steady thermal oscillation of a pulsating heat pipe, Heat & Mass Transfer 41 (2005) 685–694.
[26] R.G. Larson, N.R. Morrow, Effects of sample size on capillary pressures in porous media, Powder Technol. 30 (1981) 123–138.
[27] Z. Cao, J.L. Xu, Modulated heat transfer tube with short conical-mesh inserts: a linking from microflow to macroflow, Int. J. Heat Mass Transfer 89 (2015) 291–307.
[28] J.F. Fan, W.K. Ding, J.F. Zhang, Y.L. He, W.Q. Tao, A performance evaluation plot of enhanced heat transfer techniques oriented for energy-saving, Int. J. Heat Mass Transfer 52 (2009) 33–44.
[29] X. Zhang, Z. Liu, W. Liu, Numerical studies on heat transfer and flow characteristics for laminar flow in a tube with multiple regularly spaced twisted tapes, Int. J. Therm. Sci. 58 (2012) 157–167.
[30] T.N. Tran, Pressure Drop and Heat Transfer Study of Two-Phase Flow in Small Channels, Ph.D. Dissertation, Texas Tech University, 1998.
[31] C. Tropea. A.L. Yarin, J.F. Foss, Springer Handbook of experimental fluid mechanics, vol. 1, 2007.
[32] M.K. Dobson, J.C. Chato, Condensation in smooth horizontal tubes, J. Heat Transfer 120 (1998) 193–213.
[33] S. Laohalertdecha, S. Wongwises, The effects of corrugation pitch on the condensation heat transfer coefficient and pressure drop of R-134a inside horizontal corrugated tube, Int. J. Heat Mass Transfer 53 (2010) 2924–2931.
[34] D. Chisholm, A theoretical basis for the Lockhart-Martinelli correlation for two-phase flow, Int. J. Heat Mass Transfer 10 (1967) 1767–1778.